Unrolling the evolution kinetics of ordered SiGe islands via Ge surface diffusion

M. Grydlik,* M. Brehm,* F. Hackl, F. Schäffler, G. Bauer, and T. Fromherz†
Institut für Halbleiter- und Festkörperphysik, Johannes Kepler Universität, A-4040 Linz, Austria
(Received 7 May 2013; published 20 September 2013)

During molecular beam epitaxial growth of Ge islands on Si(001) substrates containing pit-patterned areas, an efficient Ge surface diffusion from unpatterned to pit-patterned substrate regions results in position-dependent island growth rates. We exploit this effect to map out the evolution of strictly ordered Ge islands from prepyramids via pyramids and transition domes into domes by atomic force microscopy. A one-dimensional diffusion model is established which allows a quantitative determination of the Ge surface diffusion constant and the rates at which Ge atoms are incorporated into the growing islands. We find evidence that during the shape transitions from nonfaceted islands to {105}-faceted pyramids and from pyramids to domes, Ge is incorporated at higher rates than during the growth of pure pyramids or domes. From these data it follows that a Ge atom passes on average several thousand pits before it is incorporated into one. Within our model we show that secondary-island nucleation in the substrate regions between the pits is a consequence of a mismatch between Ge incorporation and deposition rates, which results in a growing wetting layer between the ordered island sites, the thickness of which eventually exceeds the critical one for spontaneous island nucleation. We experimentally demonstrate that by lowering the Ge deposition rate, perfectly ordered islands with large pit periods of around 1 μm can be grown, in agreement with the model predictions.

DOI: 10.1103/PhysRevB.88.115311 PACS number(s): 81.07.Ta, 68.35.Fx, 81.15.Hi

I. INTRODUCTION

Interest in the growth of low-dimensional structures on predefined positions was present since the first demonstration of epitaxially grown nanostructures.[1–5] Several methods for island ordering have been investigated: selective epitaxy using openings in oxide masks,[6,7] buried stressors,[8] and pit-patterned substrates.[9–19] Using pit-patterned substrates, addressing of single islands has been demonstrated recently.[20] In the SiGe system, additionally a narrowing of the photoluminescence (PL) emission as a consequence of island ordering in pits was observed,[21] and ordered island ensembles with extremely homogeneous PL emission spectra over macroscopically large areas (3×3 mm^2) have been demonstrated.[22] In a perfectly ordered island array, exactly one island is positioned at each predefined position and no islands in-between. It has been shown that for pit-patterned substrates with pit side-wall inclination angles in the range between 5° and 18°, the preferential nucleation site of SiGe islands is at the pit bottom[16,18] where the sum of several contributions to the surface chemical potential such as strain, capillarity, facet surface energies, etc., exhibits an extremum. For the SiGe system, the relative importance of these contributions is discussed in Refs. 12 and 23. Aside from the pit side-wall inclination angle, numerous additional pit and growth parameters have to be tuned carefully with respect to each other in order to achieve perfectly ordered SiGe islands as discussed in Ref. 18 for island growth by molecluar beam epitaxy (MBE).

For nonideal growth parameters, secondary-island nucleation on the flat regions between the pits is frequently observed[24,25] and has led to the conclusion that under such growth conditions the surface diffusion length of Ge adatoms might be too short to reach the nearest nucleation site. However, Kar *et al.*[26] observed a several-μm-wide zone depleted of islands along the circumference of stripe-patterned substrate regions from which Ge adatoms diffuse into the patterned fields, indicating a surface diffusion length much larger than the typical interpit distances. Similarly, large surface diffusion lengths were observed for InAs on GaAs substrates at typical island growth temperatures.[27]

The adatoms diffusing into the patterned region increase the supply of deposited material provided homogeneously via the deposition rate and result in an enhanced growth rate of the islands close to the border between patterned and unpatterned regions.[26,27] It is therefore evident that the observed spatial decay of the island volumes depends both on the surface diffusion constant as well as on the efficiency of the growing islands as sinks for the surface diffusing species. However, no experimental quantification of this efficiency nor any correlation of it to the shape of the island exists so far in literature. This is surprising since, on the one hand, the knowledge of these parameters might be extremely important as an input for molecular dynamic modeling of the island growth processes. On the other hand, from an experimental point of view, we show in this paper that a quantitative knowledge of these parameters allows a predictive further optimization of the island growth conditions to achieve perfect island ordering also on substrates with large pit periods.

The paper is organized as follows: In Sec. II, the growth conditions and the setup for atomic force microscopy (AFM) used for the determination of the island shapes and the setup for measuring their photoluminescence (PL) emission are described. In Sec. III, the experimental results of AFM and PL experiments, and in Sec. IV the modeling of the combined Ge surface diffusion and SiGe island growth, are presented. In Sec. V, the outcome of the modeling is compared to the experimental results. The Ge surface diffusion constant and the Ge incorporation rates of prepyramids, pyramids, transition domes, and domes are determined, and it is shown that diffusing Ge atoms visit on average more than 10 000 pits before being incorporated into a growing island. The consequences of these findings on further optimizing the growth parameters are discussed. In the Appendix, details on the numerical solution of the diffusion model are described.

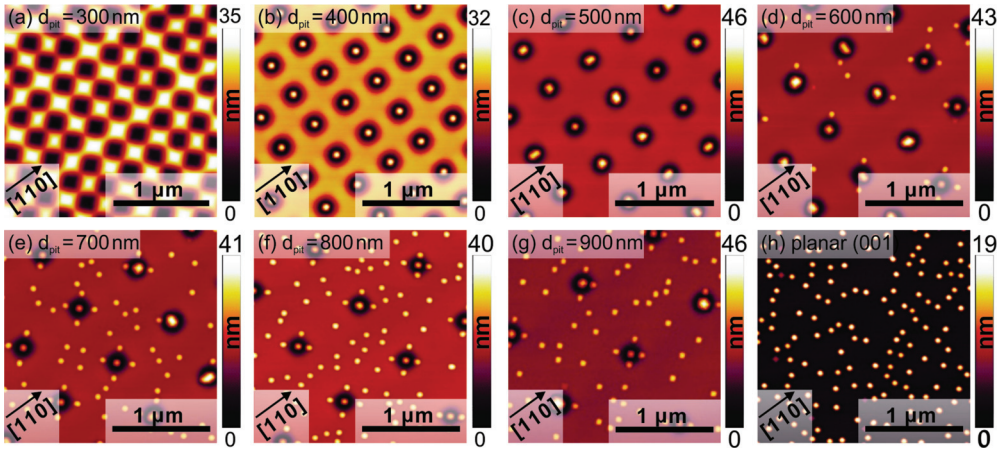

FIG. 1. (Color online) AFM micrographs of islands nucleated in the center of the patterned fields with d_{pit} in the range between 300 and 900 nm as given by the labels of panels (a)–(g) and on the unpatterned part of the substrate [(h)]. The detailed growth conditions are described in the text.

II. EXPERIMENTAL PROCEDURE

We fabricated pit-patterned fields with the size of 200 × 200 μm^2 by standard electron-beam lithography and subsequent reactive ion etching on high-resistivity (500–5000 Ω cm) Si(001) substrates. On two samples, seven fields with pit periods (d_{pit}) from 300 to 900 nm in steps of 100 nm were realized. The dimensions of the cylindrical pits before growth were 50 nm in depth and 200 nm in width. After patterning, the substrate was cleaned and transferred into a Riber SIVA45 solid source MBE chamber and *in situ* degassed at 700 °C for 45 min. Hereafter, a 45-nm-thick Si buffer layer was grown at a rate of 0.6 Å/s and a growth temperature ramp-up from 450 °C to 550 °C.

After a growth interrupt of 15 s, during which the substrate temperature was ramped up to $\theta_g = 650$ °C, 8.4 Å (∼6 monolayer, ML) of Ge were deposited at a Ge growth rate of 0.025 Å/s. Thus, the total growth time t_{tot} was 330 s. To allow the *ex situ* characterization of the island properties by a nanoscope atomic force microscope (AFM) in tapping mode, for one sample the growth sequence was stopped after the Ge deposition. Another sample used for microphotoluminescence spectroscopy (μ-PL) was additionally overgrown with a 50-nm-thick Si cap, deposited at a growth rate of 0.6 Å/s and a temperature of 300 °C. It was shown that growth at 300 °C prevents SiGe intermixing during the capping layer growth process.[28–31] The μ-PL measurements were conducted at a temperature of 10 K under excitation by a frequency-doubled Nd:YAG laser with a wavelength of 532 nm, an intensity of 20 kW/cm^2, and a spatial resolution of 5 μm.

III. RESULTS

Figure 1 shows AFM micrographs of islands which nucleated in the center of the pit-patterned fields with d_{pit} in the range between 300 and 900 nm as given in the panel labels [Figs. 1(a)–1(g)] and, for comparison, on the unpatterned part of the substrate [Fig. 1(h)]. It is evident that the shapes and the volumes of the islands in the pits and the degree of the island ordering depend crucially on the pit period d_{pit}. Whereas for $d_{pit} = 300$ nm no upright islands in the pits are present, for $d_{pit} = 400$ nm perfectly ordered domes with a homogeneous size distribution are observed. For further increased values of d_{pit} from 500 to 900 nm, the domes in the pits tend to evolve to dislocated superdomes[24,32] with an asymmetric shape. In addition, secondary-island nucleation in the flat substrate regions between the pits occurs for $d_{pit} \geqslant 600$ nm.

Sections of the border regions between unpatterned and pit-patterned regions of the substrate are presented in Fig. 2. Outside the patterned region, zones depleted of islands are

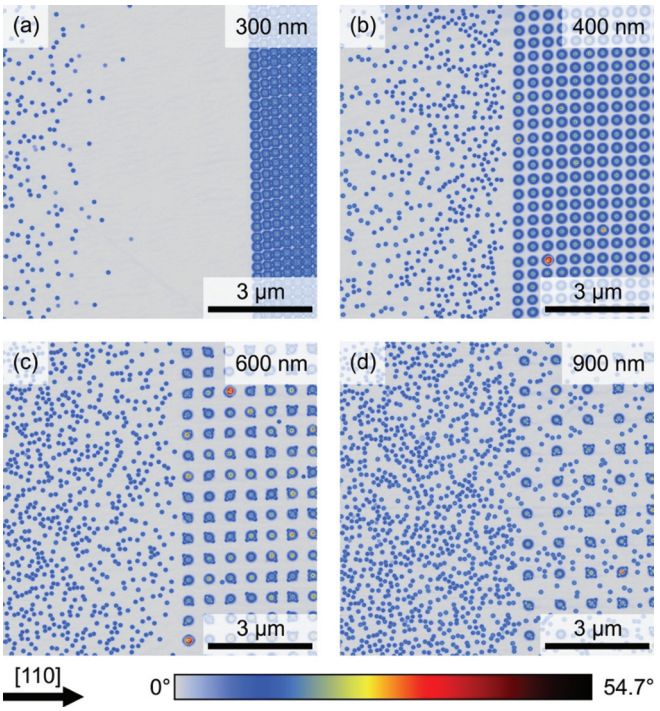

FIG. 2. (Color online) 10 × 10 μm^2 AFM micrographs taken in the vicinity of the border between unpatterned and patterned substrate regions with (a) $d_{pit} = 300$ nm, (b) 400 nm, (c) 600 nm, and (d) 900 nm. The color coding represents the local surface slope with respect to the (001) surface.

observed, the width of which strongly depends on d_{pit}. The depleted zones are several micrometers wide for $d_{pit} = 300$ nm, less than 1 μm for $d_{pit} = 400$ nm, and virtually absent for $d_{pit} = 600$ and 900 nm. The existence of depleted zones adjacent to regions with ordered islands was observed previously both for the SiGe and the InAs/GaAs system.[26,27] However, the strong dependence of its width on the pattern period was not reported so far. In Refs. 26, 27 the formation of these depleted zones is ascribed to material flow via surface diffusion into the patterned substrate regions, where pits or stripes act as preferential island nucleation centers and, thus, as material sinks.

The material diffusion towards the centers of the patterned areas has to be sustained by a gradient in the areal concentration of mobile Ge atoms on the wafer surface. Thus, close to the border between the unpatterned and pit-patterned substrate region, more Ge is available for island formation than in the center of the patterned fields. As a consequence, inside the patterned fields in the vicinity of the border the islands are further developed as compared to the center of the patterned field. This is most prominently observable for the $d_{pit} = 300$ nm field on our substrate, for which also the zone depleted of islands is the broadest. The various panels of Fig. 3 show the different island shapes that are found as the distance x (specified by the labels) to the border between unpatterned and pit-patterned substrate regions decreases for Figs. 3(a) to 3(f) from 55 to 0.3 μm, respectively. Note that for this field no *upright* islands are observed in the pits in the middle of the field, i.e., 100 μm away from any border to the unpatterned part of the sample [Fig. 1(a)]. Therefore, we conclude that, far away from any border, for this pattern period and the pit shape as described in Sec. II, 6 ML of deposited Ge is just enough to decorate the pit sidewalls by {105} facets and establish a flat (001) base at the bottom of the pits,[18,33] as shown in the three-dimensional AFM micrograph in Fig. 3(a). In the corresponding surface orientation map[34,35] (SOM) in the right panel of Fig. 3(a), only {105} spots are pronounced, one representative of which is marked by a triangle.

Approaching the border of the $d_{pit} = 300$ nm field (position $x = 0$) along a line perpendicular to this border through the center of the field, the island shapes shown in Fig. 3 for various positions x are observed: inside the field at $x = 42$ μm we observe small convex structures in the pits. As a consequence of the pit inclination angle being in the range between 5° and 18°,[16,18] these unfaceted structures, commonly called prepyramids or mounds,[36] are all located in the center of the pit [Fig. 3(b)]. At a distance from 30 μm to 7 μm we observe {105}-faceted pyramidal islands.[3] The volume of these pyramids increases as x decreases towards the border.

At $x = 3$ μm we observe so-called transition domes [see Fig. 3(e)].[37,38] These are islands that exhibit facets already steeper than the {105} ones of the pyramids (i.e., {113} and/or {15 3 23}), but do not have all facets of a dome[39] in all ⟨110⟩ and ⟨510⟩ directions. Additional points in the SOM of Fig. 3(e) indicate those additional facets. Finally, at $x = 0.3$ μm fully evolved multifaceted domes[39] [Fig. 3(f)] are observed. The SOM in Fig. 3(f) clearly indicates the {113} and {15 3 23} high-index dome facets in all respective ⟨110⟩ and ⟨510⟩ directions.

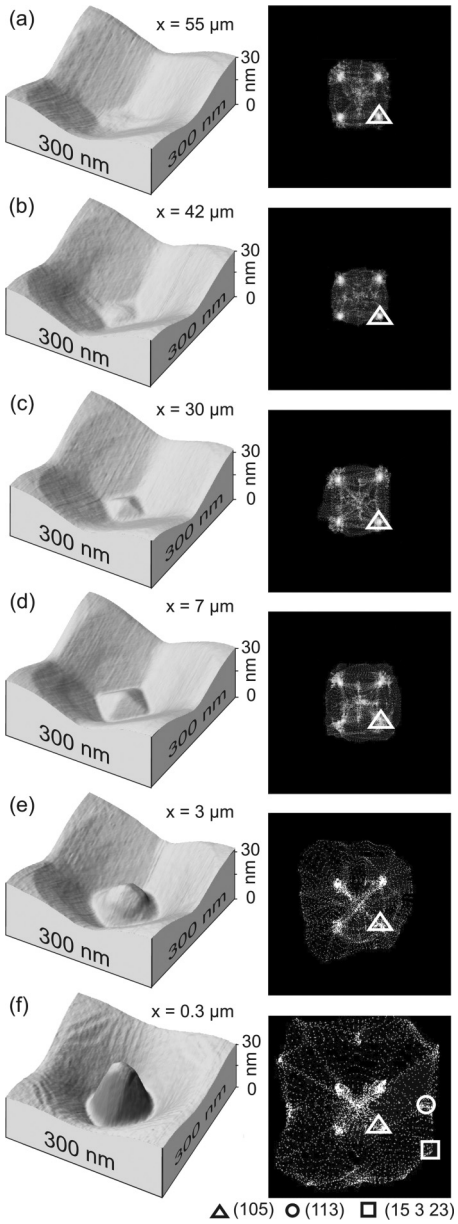

FIG. 3. Left column: Three-dimensional AFM micrographs (300×300 nm^2) taken on the field with $d_{pit} = 300$ nm. Various pit-surface morphologies [facet formation (a), prepyramids (b), pyramids (c) and (d), transition domes (e), and domes (f)] are observed for the different distances x (specified by the panel labels) from the border between unpatterned and pit-patterned substrate regions. The corresponding surface orientation maps are shown in the right column. The dome facets {105}, {113}, and {15 3 23} are marked by triangles, circles, and squares, respectively.

More detailed information on the position-dependent island morphology across the border between unpatterned and pit-patterned substrate regions is given in the Supplemental Material,[40] where overlapping 1.8×1.8 μm^2 AFM micrographs are combined to a 90×1.8 μm^2 large image covering the region -42 μm $< x <$ 48 μm. A summary of this plot is shown in Fig. 4, where the average island volume V_{av}^{300} is plotted on a logarithmic scale against the position x for -42 μm $< x <$ 48 μm. The island volume was evaluated from

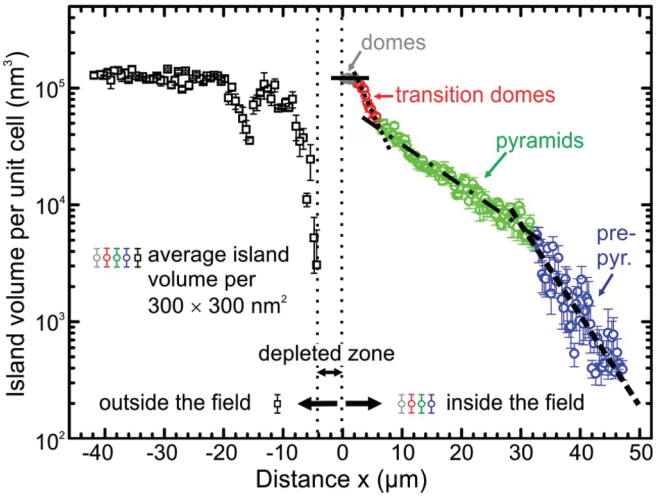

FIG. 4. (Color online) Average island volume per 300 × 300 nm^2 unit cell V_{av}^{300} as a function of the distance from the border between the unpatterned and pit-patterned parts of the sample. The 4.4-μm-wide depleted region where no islands are present is marked by two vertical dotted lines. The solid, dotted, dashed-dotted, and dashed lines indicating an exponential decrease of island volume with distance with different decay length for transition domes, pyramids, and prepyramids.

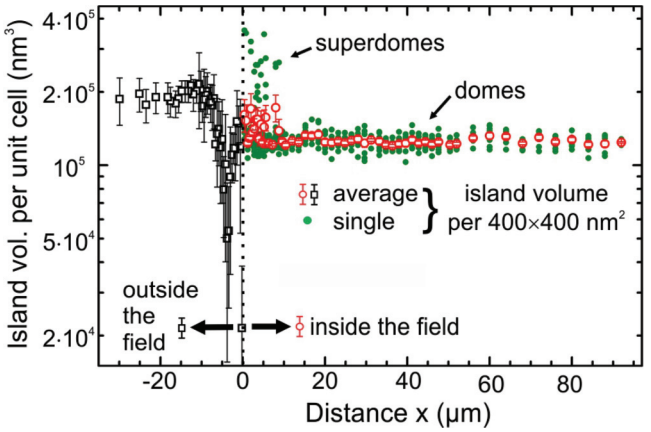

FIG. 5. (Color online) Island volume per 400 × 400 nm^2 unit area as a function of the distance from the border between the unpatterned and pit-patterned parts of the sample. The black open squares are V_{av}^{400} on the unpatterned part of the sample, while the empty red circles mark the values for V_{av}^{400} on the pit-patterned part. To show the narrow size uniformity of the domes, we plotted the volumes of the single islands (full green circles) too. Dislocated superdomes with volumes larger than 1.4 × 10^5 nm^3 are observed for 0 μm > x > 10 μm (see also Fig. 2).

the island facets protruding from the pits ($x > 0$) or the WL surface ($x < 0$) as observed in the AFM micrographs assuming a flat island base. Inside the patterned region, we determined V_{av}^{300} and the corresponding error bars from at least five islands per pit column at fixed $x = nd_{pit}$, where n is an integer number and $d_{pit} = 300$ nm. Outside the patterned area, the volume of all islands within a cell as large as the pattern unit cell was summed up. This sum was then averaged over five cells and the resulting value V_{av}^{300} is plotted in Fig. 4 for $x < 0$.

From Fig. 4 it is evident that inside the patterned field, V_{av}^{300} decays exponentially with four different decay lengths represented by the slopes of the full, dotted, dashed-dotted, and dashed straight lines. From a comparison with the island shapes observed by AFM at $x = nd_{pit}$,[40] the different regions of constant volume decay length can be attributed to the different stages of the island development, i.e., to domes, transition domes, pyramids, and prepyramids, as presented in Fig. 3. The volume decay length can be taken as a measure for the probability that a diffusing Ge atom is incorporated into an island, where a smaller decay length corresponds to a larger probability (a quantitative discussion of this correspondence is given in Sec. IV and in the Appendix). Thus, from Fig. 4 we conclude that for the transition island shapes with incomplete facets (prepyramids and transition domes), the probability for Ge incorporation is significantly larger than for the pyramids with fully developed {105} facets. In addition, for the completely evolved domes present close to the border, a virtually vanishing Ge incorporation probability is observed, indicating that these islands are exceptionally stable against further volume enlargement.[41]

Outside the patterned region far from the border ($-42\ \mu\text{m} < x < -22\ \mu\text{m}$), $V_{av}^{300} = 1.25 \times 10^5$ nm^3 is observed independently of x. For $-8.4\ \mu\text{m} < x < -4.4\ \mu\text{m}$, V_{av}^{300} decreases towards zero. The depleted region where no islands exist is marked in Fig. 4 by the two vertical dotted lines at $x = 0\ \mu$m and $x = -4.4\ \mu$m. In addition, a very pronounced dip in V_{av}^{300} for $-19\ \mu\text{m} < x < -13\ \mu\text{m}$ is observed, the origin of which is discussed in Sec. IV.

For the $d_{pit} = 400$ nm field, domes are observed also in the center of the patterned field [see Fig. 1(b)]. The detailed dependence of the average island volume V_{av}^{400} (determined in analogy with V_{av}^{300}) on the position x is shown in Fig. 5 on a logarithmic ordinate axis. Between $x = 10\ \mu$m and the center of the quadratic field at $x = 100\ \mu$m, a constant island volume of 1.24 × 10^5 nm^3 is observed. A comparison with Fig. 4 shows that this is exactly the volume also observed for the domes in the $d_{pit} = 300$ nm field close to the border between the unpatterned and pit-patterned regions. This finding is a further indication that for the pit geometry used in this work, ordered domes become stable against volume increase at a volume around 1.24 × 10^5 nm^3. Once this volume has been reached, Ge is not further incorporated into domes but diffuses to regions of islands with a finite incorporation probability (transition domes, pyramids, prepyramids) where it is consumed during the evolution of these islands into domes. From our results we conclude that it is the domes' stability against volume enlargement that leads from a strongly position-dependent island volume distribution as shown in Fig. 4 to an island volume constant over large areas, provided that sufficient Ge is deposited to form fully developed domes at all array sites. In Sec. IV, a quantitative model is developed based on these findings.

In Figs. 2(b) and 5, at the border between the unpatterned and pit-patterned regions, a much narrower, nearly vanishing region of reduced island density in the unpatterned region is observed for the $d_{pit} = 400$ nm field as compared to the $d_{pit} = 300$ nm field shown in Figs. 2(a) and 4. In addition, in the patterned region for $0 < x < 10\ \mu$m a significant number of dislocated superdomes with volumes $\geqslant 2 \times 10^5$ nm^3 is

observed. In Sec. IV, we show that once ordered domes have formed close to the border between unpatterned and pit-patterned substrate regions, the Ge incorporation probability vanishes in these regions. As a consequence, there the areal concentration of mobile Ge atoms exhibits a local maximum. This results in Ge diffusion from the region close to the border also into the unpatterned region, speeding up the growth of wetting layer (WL) and islands there, as well as the formation of dislocated superdomes in the patterned region with fully evolved domes.

For applications of ordered islands, for example in integrated optics,[42] the spatial homogeneity of the islands' optoelectronic properties is of crucial importance. We thus investigated the islands' PL emission spectra as a function of the distance from the border. For the PL experiments, the islands were grown under nominal identical growth conditions as those shown in Figs. 4 and 5. In addition, a 50-nm Si cap layer was deposited at 300 °C after the island growth for suppressing surface recombination of electron-hole pairs bound to the islands and the WL. The low capping layer growth temperature prevents Si/Ge intermixing[28–31] and assures that the Si capping layer grows in a conformal way on the Ge island.[29,31] Due to an incidental small increase of the Ge rate, slightly more Ge was deposited on the capped sample than on the uncapped sample. This extra material of a few tenths of a ML was sufficient to create small pyramids also in the center of the 200 × 200 μm^2 field with $d_{\mathrm{pit}} = 300$ nm, as evidenced by AFM images (not shown).

Figure 6 shows a contour plot derived from μ-PL spectra recorded in steps of $\Delta x = 2$ μm for -32 μm $< x <$ 23 μm. The color coding represents the PL intensity where dark blue and red depict low and high intensities, respectively. Since the detection area has a diameter of 5 μm, the areas overlap spatially, however, regions with different morphologies can be clearly distinguished in the contour plot.

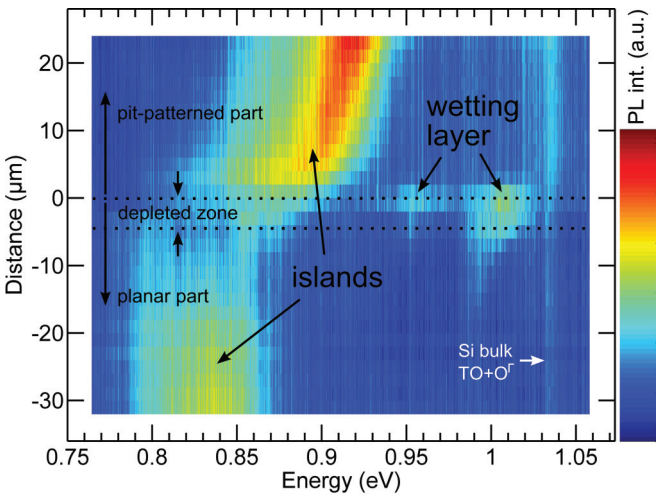

FIG. 6. (Color online) Contour plot of μ-PL spectra as a function of the distance x from the border between the unpatterned and pit-patterned ($d_{\mathrm{pit}} = 300$ nm) substrate regions at $x = 0$ μm. PL signals originating from the islands and the wetting layer are indicated by arrows. A strong increase of the island PL intensity as well as a shift to higher energies is observed for $x > 0$ μm due to the changing island morphology.

The peak at 1.035 eV, present at all positions in Fig. 6, originates from the Si bulk TO + O$^{\Gamma}$ two-photon replica.[43] In the PL spectra taken at positions -32 μm $< x < -5$ μm the dominant signal is a broad peak between 0.78–0.87 eV stemming from the islands nucleated randomly on the unpatterned part of the substrate.[21,44] For -15 μm $< x < 0$ μm, the intensity of this island signal decreases concomitantly with an increase of the wetting layer band observed between 0.94 and 1.03 eV. The wetting layer band consists of several peaks. The most pronounced ones are the no-phonon assisted peak (WL-NP) at about 1.01 eV and the transverse optical (TO) Si-Si phonon assisted peak at about 0.95 eV. In the depleted region between -5 μm $< x < 0$ μm, the WL-NP emission peak shifts from 1.00 to 1.01 eV. According to Refs. 30 and 44, this shift is caused by a decrease of the WL thickness from 3.1 to 2.9 ML. The most intense PL signal is observed in Fig. 6 for the ordered islands at $x > 0$ between 0.82 and 0.95 eV. As the islands become smaller with increasing x (see Figs. 3 and 4), the island PL emission shifts significantly towards higher energies. The large domes at $x = 0.3$ μm emit most intense at 0.87 eV, while the prepyramids at $x \approx 23$ μm show an emission maximum at 0.92 eV. Figure 6 shows that the integrated PL intensity originating from the prepyramids at $x \approx 23$ μm is strongly enhanced as compared to the one of both the ordered dome islands between $0 < x < 0.3$ μm and the randomly nucleated islands at $x < -5$ μm. This PL enhancement is tentatively ascribed to an increased quantum confinement in the prepyramids (height: ∼2–3 nm) as compared to the domes (height: ∼30–40 nm).

IV. MODELING

For a quantitative understanding of the dependence of the island shapes on the position on the substrate and the Ge flow between unpatterned and pit-patterned regions of the substrate, the two-dimensional surface diffusion equation

$$\left[\frac{\partial}{\partial t} - D\left(\frac{\partial^2}{\partial x^2} + \frac{\partial^2}{\partial y^2}\right)\right] n(x,y,t) = R - \eta(x,y,t) \qquad (1)$$

has to be solved. Here, x, y are the coordinates of a point on the substrate where the unit vectors $\vec{e}_x, \vec{e}_y$ are chosen parallel to the pit array basis vectors. $n(x,y,t)$ is the position-dependent surface concentration of mobile Ge atoms at time t, D the surface diffusion constant, R the deposition flux that adds mobile Ge atoms to $n(x,y,t)$, and $\eta(x,y,t)$ the flux of Ge atoms incorporated into the growing islands (incorporation flux). Since $\eta(x,y,t)$ varies within a pattern unit cell, so does $n(x,y,t)$. However, no experimental data are available indicating the variation of n within a unit cell. Therefore, we average Eq. (1) over a unit cell by replacing n and η in Eq. (1) with the average values $\bar{n}$ and $\bar{\eta}$ defined according to $\bar{c} \equiv \frac{\int_u c\, dA}{A_u}$, where A_u denotes the area of a unit cell u and c stands for n or η.

In the following, we restrict our analysis to substrate areas in the vicinity of the border line between the unpatterned and pit-patterned fields perpendicular to the x direction but far away from the border line perpendicular to the y direction. Thus, the dependence of $\bar{n}$ on y can be neglected and the averaged diffusion equation becomes one dimensional:

$$\left[\frac{\partial}{\partial t} - D\left(\frac{\partial^2}{\partial x^2}\right)\right] \bar{n}(x,t) = R - \bar{\eta}(x,t). \qquad (2)$$

In order to be able to solve Eq. (2), a model for $\bar{\eta}$ has to be established. We assume that the differential probability dW with which a Ge atom is incorporated into an island within the time interval dt can be expressed as

$$dW = S_i dt, \tag{3}$$

where S_i denotes the Ge incorporation probability density that depends only on the island type i ($i \in \{d, td, p, pp\}$ for domes, transition domes, pyramids, and prepyramids, respectively) as concluded from the results shown in Fig. 4. The differential probability can also be expressed as

$$dW = -d\bar{n}/\bar{n}, \tag{4}$$

where $d\bar{n}$ denotes the number of Ge atoms incorporated per unit-cell area into a growing island within the time interval dt, i.e.,

$$d\bar{n} = -\bar{\eta}\, dt. \tag{5}$$

Combining Eqs. (3) and (4) using Eq. (5) results in

$$\bar{\eta} = \bar{n} S_i. \tag{6}$$

Inserting Eq. (6) into Eq. (2) results in a partial differential equation for $\bar{n}(x,t)$ with a spatial constant inhomogeneous part R:

$$\left[\frac{\partial}{\partial t} - D\left(\frac{\partial^2}{\partial x^2}\right) + S_i\right]\bar{n}(x,t) = R. \tag{7}$$

By introducing the dimensionless variables

$$\nu := \bar{n}/n_{\text{tot}}, \quad \tau := t/t_{\text{tot}}, \quad \xi := x/L, \quad \sigma_i := S_i t_{\text{tot}}, \tag{8}$$

where n_{tot} is the totally deposited Ge surface coverage, t_{tot} the total growth time, i.e., $R = n_{\text{tot}}/t_{\text{tot}}$ and $L := \sqrt{t_{\text{tot}} D}$ the diffusion length, Eq. (7) is simplified and becomes

$$\left[\frac{\partial}{\partial \tau} - \left(\frac{\partial^2}{\partial \xi^2}\right) + \sigma_i\right]\nu(\xi,\tau) = 1. \tag{9}$$

Far away from any border, the spatial derivative term in Eq. (9) vanishes and a solution for $\nu(\tau)$ is obtained that exponentially approaches its stationary value $1/\sigma_i$ with a decay constant $\tau_i := 1/\sigma_i$. In such exponential growth or decay processes, the decay constant denotes an average (normalized) lifetime. Thus, in our case $T_i := \tau_i t_{\text{tot}}$ can be interpreted as the average surface diffusion time of a Ge WL atom after which it is incorporated into a SiGe island.

In regions where the diffusion term in Eq. (9) is finite, the solution of Eq. (9) is obtained numerically as outlined in the Appendix. From the distinct volume decay lengths evident in Fig. 4 it is clear that inside the patterned field at critical values $V_c^{i,j}$ of the island volumes V_{av}^{300} at which the shape transitions occur, the scaled incorporation probability density changes from σ_i to σ_j ($\sigma_{pp} \to \sigma_p$ at $V_c^{pp,p} = 5 \times 10^3$ nm^3, $\sigma_p \to \sigma_{td}$ at $V_c^{p,td} = 4.9 \times 10^4$ nm^3, $\sigma_{td} \to \sigma_d$ at $V_c^{td,d} = 1.21 \times 10^5$ nm^3). These experimental findings are included in our simulation by integrating over the Ge incorporation rate to calculate $V_{\text{av}}^{300}(\xi,\tau)$ according to

$$V_{\text{av}}^{300}(\xi,\tau) = V_c^{i,j} + \frac{n_{\text{tot}} A_u a^3_{\text{Si}_{1-\bar{c}}\text{Ge}_{\bar{c}}}}{8\,\bar{c}} \int_{\tau^{i,j}(\xi)}^{\tau} \nu(\xi,\tau')\sigma_j(\xi) d\tau', \tag{10}$$

where $\bar{c}$ denotes the average Ge concentration of an island as determined by x-ray diffraction measurements ($\bar{c} = 0.5$) (Ref. 45) and $a_{\text{Si}_{1-\bar{c}}\text{Ge}_{\bar{c}}}$ the corresponding alloy lattice constant. $V_c^{i,j}$ is the largest element out of $\{V_c^{pp,p}, V_c^{p,td}, V_c^{td,d}\}$ that is still smaller or equal to $V_{\text{av}}^{300}(\xi,\tau)$, and $\tau^{i,j}(\xi)$ denotes the normalized time at which $V_{\text{av}}^{300}(\xi,\tau)$ has reached $V_c^{i,j}$ at position ξ, i.e., $V_{\text{av}}^{300}[\xi, \tau^{i,j}(\xi)] = V_c^{i,j}$. In the simulation, at $\tau^{i,j}(\xi)$ we replace σ_i by σ_j at position ξ (for a more detailed discussion, see the Appendix).

On the unpatterned part of the substrate, dome formation occurs via the assembly of a WL with overcritical thickness and a subsequent spontaneous island nucleation fueled by a Ge transfer from the WL to the growing islands as described in Ref. 44. In our simulations, we model these experimental findings by a WL Ge incorporation probability density σ_{WL} that decreases linearly from its maximum value $\sigma_{\text{WL}}^{\max}$ at the WL thickness $h_{\text{WL}} = 0$ to $\sigma_{\text{WL}} = 0$ for a maximum WL thickness $h_{\text{WL}} = h_{\text{WL}}^{\max}$ which was determined in Ref. 44 to be $h_{\text{WL}}^{\max} \sim$ 3–5 ML. The WL thickness $h_{\text{WL}}(\xi,\tau)$ is calculated in analogy with Eq. (10) by

$$h_{\text{WL}}(\xi,\tau) = \frac{V_{\text{av,WL}}^{300}(\xi,\tau)}{A_u} = \frac{n_{\text{tot}} a^3_{\text{Ge}}}{8} \int_0^{\tau} \nu(\xi,\tau')\sigma_{\text{WL}}(\xi) d\tau', \tag{11}$$

where the lattice constant of Ge (a_{Ge}) is used, as it has been shown that at the employed growth conditions the Ge concentration in the WL is larger than 85%.[30]

The linear approximation of the decrease of σ_{WL} with h_{WL} is inspired by the linear dependence of the island growth rate on the chemical potential of Ge atoms used in Ref. 46 and the almost linear increase of the Ge atoms' chemical potential in a Ge layer on a Si(001) substrate with increasing layer thickness up to 3 ML.[47] In order to include the WL thinning into our model, we define $h_{\text{WL}}^{\max}$ as the maximum value of $h_{\text{WL}} + h_{\text{Ge}}$ above which dome nucleation sets in, i.e., at which σ_{WL} is replaced by $\sigma_{d^{\text{up}}}$, where h_{Ge} denotes the film thickness of the not yet incorporated Ge [$h_{\text{Ge}}(\xi,\tau) = V_{\text{av,Ge}}^{300}(\xi,\tau)/A_u = \nu(\xi,\tau) n_{\text{tot}} a^3_{\text{Ge}}/8$] and $\sigma_{d^{\text{up}}}$ the scaled Ge incorporation probability density for domes on the unpatterned substrate regions.

V. DISCUSSION AND CONCLUSIONS

For a given set of the scaled incorporation probability densities σ_i for the islands in and outside the patterned field regions as well as for the WL outside the patterned field, Eq. (9) is solved numerically for $\nu(\xi,\tau)$ as outlined in the Appendix. The volumes of the islands are calculated using Eq. (10). For a comparison with the observed position dependence of $V_{\text{av}}^{300}(x, t_{\text{tot}})$ as shown in Fig. 4, the diffusion length L has to be specified, too. Thus, within the Levenberg-Marquardt algorithm,[48] L, $h_{\text{WL}}^{\max}$, $\sigma_{\text{WL}}^{\max}$, σ_{td}, σ_p, σ_{pp}, and $\sigma_{d^{\text{up}}}$ were treated as fitting parameters to simulate the experimentally observed $V_{\text{av}}^{300}(x, t_{\text{tot}})$ profile by the model described in the previous section. For the ordered domes, a constant volume independent of the distance from the border between unpatterned and pit-patterned substrate regions was experimentally observed. Thus, the corresponding scaled probability density σ_d was set to 0.

TABLE I. Ge surface diffusion constant D and Ge incorporation probability densities S for the different island types and the WL as obtained from fitting the experimentally observed dependence of the island volumes on the distance from the border between unpatterned and pit-patterned ($d_{\mathrm{pit}} = 300$ nm) substrate areas for a growth temperature of 650 °C. The diffusion times T, the diffusion radii R, and the average number of pits N visited by a Ge atom during its diffusive random surface walk are calculated from S and D as described in the text.

Surface morphology		S (s^{-1})	T (s)	R (μm)	N
Patterned substrate ($d_{\mathrm{pit}} = 300$ nm)	Transition domes	0.097	10.31	19.4	13200
	Prepyramids	0.113	8.82	17.9	11200
	Pyramids	0.027	37.59	37.0	47900
Unpatterned substrate	Rand. nuc. islands	0.031	32.35	34.4	70400
	WL	$0.018 \rightarrow 0$ (ML: $0 \rightarrow h_{\mathrm{WL}}^{\mathrm{max}}$) $h_{\mathrm{WL}}^{\mathrm{max}} = 2.4$ ML	54.16 ($\rightarrow \infty$)	42.5 ($\rightarrow \infty$)	
Patterned and unpatterned substrate	Ge atoms	Surface diffusion constant: $D = 4.56\ \mu\mathrm{m}^2/\mathrm{s}$			

The absence of islands in the center of the field with 300-nm period [see Fig. 1(a)] indicates that for this field at least 6 ML of Ge are consumed for the exposure of the facets which develop at the the pit side walls. In our simulations, we did not explicitly distinguish between prepyramid and facet formation because we have no experimental data on the x dependence of the amount of Ge stored in the facets. The measured island volumes on the patterned fields do not contain the Ge consumed for the formation of the side-wall facets of the pits. Therefore, in the fitting routine we simulate $V_{\mathrm{av}}^{300}(x,t_{\mathrm{tot}}) - V_{\mathrm{av}}^{300,\ \mathrm{center}}(t_{\mathrm{tot}})$ and fit it to the experimentally observed volumes, where $V_{\mathrm{av}}^{300,\ \mathrm{center}}(t_{\mathrm{tot}})$ denotes the incorporated Ge in the center of the patterned field far away from its border.

Our simulations show that on the unpatterned substrate region between $-10\ \mu\mathrm{m} < x < 0\ \mu\mathrm{m}$, the steep decrease of the island volume and the width of the region depleted of islands shown in Fig. 4 depend both on the scaled WL Ge incorporation probability density $\sigma_{\mathrm{WL}}^{\mathrm{max}}$ as well as on the maximum WL thickness $h_{\mathrm{WL}}^{\mathrm{max}}$. Thus, these parameters can be determined by the fitting procedure and the volumes of the islands on top of the WL can be simulated separately from the WL. For the unpatterned substrate region, a comparison with the measured island volumes is therefore possible without the necessity to subtract an offset volume corresponding to $V_{\mathrm{av}}^{300,\ \mathrm{center}}(t_{\mathrm{tot}})$, which had to be subtracted from the simulated island volumes on the patterned substrate regions.

The values for the incorporation probability densities S_i, the maximum WL thickness $h_{\mathrm{WL}}^{\mathrm{max}}$, and the Ge surface diffusion constant D obtained by the fitting procedure are listed in Table I. The simulated island volume as a function of the distance from the border between patterned and unpatterned substrate regions is shown in Fig. 7(a) by the solid line. Excellent agreement with the measured values shown by the symbols in Fig. 7(a) is achieved.

For the following discussion, it is helpful to calculate the number of pits (N_i) a diffusing Ge atom visits on average during its lifetime T_i on a patterned substrate with island type $i \in \{td, p, pp\}$. The Ge atom performs a diffusive random surface walk $\ell(t)$, where the variance $\Delta\ell^2$ is related to the diffusion constant by the two-dimensional Einstein relation for Brownian motion $\Delta\ell^2 = 4DT_i$. Since for a random walk restricted to a circle with radius R a variance $\Delta\ell^2 = R^2/2$ (assuming that each point within the circle is visited with the same probability) is calculated, we can visualize the range of the diffusive surface motion of a single Ge atom by a circle with radius

$$R_i = \sqrt{8DT_i}\,. \tag{12}$$

In Table I, the radii R_i are given for the various island types for the patterned field with 300-nm period. In the last column of Table I, we list the number of pit sites N_i that a Ge atom

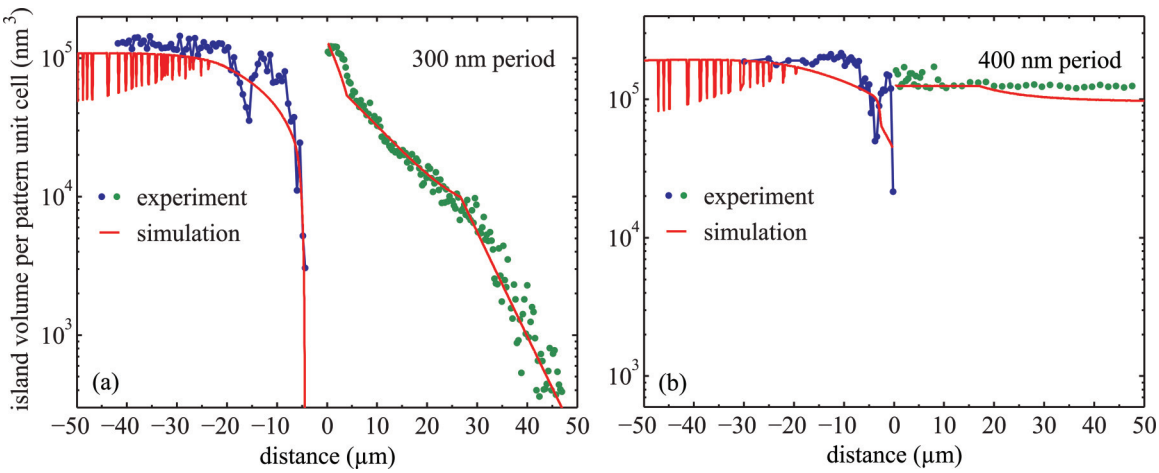

FIG. 7. (Color online) Island volume versus distance x from the border of the fields patterned with 300-nm (a) and 400-nm (b) pit period. Comparison between the experimental results and the simulations are corrected for the volumes stored in the pit facets and the wetting layer.

visits on average in a substrate region with island type i before it is incorporated. These values are calculated using

$$N_i = R_i^2 \pi \big/ A_u = \frac{8D\pi}{S_i A_u}, \tag{13}$$

where for the last equality we have used Eq. (12) and $T_i = 1/S_i$ as defined in the context of Eq. (9). For calculating $N_{d^{up}}$ for the islands outside the patterned field, the unit-cell area A_u in Eq. (13) was replaced by $1/\rho$, where ρ is the island density ($\rho = 1.9 \times 10^9$ cm^{-2}).

If we assume vanishing Ge incorporation in the areas between the pits as well as a Ge surface diffusion constant and pit properties independent of A_u, the values for N_i given in Table I have to be independent of d_{pit}. Under these assumptions, it follows from Eq. (13) that also $S_i A_u$ has to be independent of $A_u = d_{pit}^2$ and, thus, $S_i \propto 1/d_{pit}^2$. This scaling behavior of the incorporation probability densities S_i is, of course, a consequence of the averaging of the diffusion equation over A_u leading to Eq. (2) and is in agreement with the experimental findings reported in Ref. 18. The values for S_i given in Table I were thus rescaled and used to simulate the island volumes V_{av}^{400} for the field with $d_{pit} = 400$ nm as shown in Fig. 7(b). For the comparison between measured and simulated volumes in the patterned substrate area, the Ge consumed for pit-facet covering has to be considered, as discussed already for the $d_{pit} = 300$ nm field. For the $d_{pit} = 400$ nm field, we scaled down $V_{av}^{300,center} = 6$ ML, which we assumed was being used for facet covering for the $d_{pit} = 300$ nm field by the ratio of the unit-cell areas, i.e., by $\frac{9}{16}$ and subtracted this value (3.375 ML) from the simulated volume. Under this assumption, the observed dome volume inside the $d_{pit} = 400$ nm field (1.3×10^5 nm^3) and the simulated one at the border are equal, as shown in Fig. 7(b). The good agreement also with the observed spatial variation of the island volume shown in Fig. 7(b) confirms the significance of the parameters listed in Table I for the growth conditions and pit shapes of our experiments. However, we want to point out that our data do not reveal any microscopic factors that determine the Ge incorporation probability densities S_i. Aside from the growth temperature, it may be expected that the magnitude of the strain field surrounding an island significantly influences the probability for the incorporation of a Ge adatom into a growing island and, thus, the values of S_i.

To gain insight into the island evolution, the end point of which is shown in Fig. 7 for $d_{pit} = 300$ and 400 nm, in Fig. 8 the incorporation probability density profiles (upper panels), the averaged Ge surface concentration profiles (middle panels), and the WL and island volume profiles (bottom panels) are shown at three different instants during the Ge deposition time ($t = 0.3, 0.55, 1 \times t_{tot}$, for a movie showing the complete time evolution between $\tau = 0$ and 1, see Supplemental Material[40]).

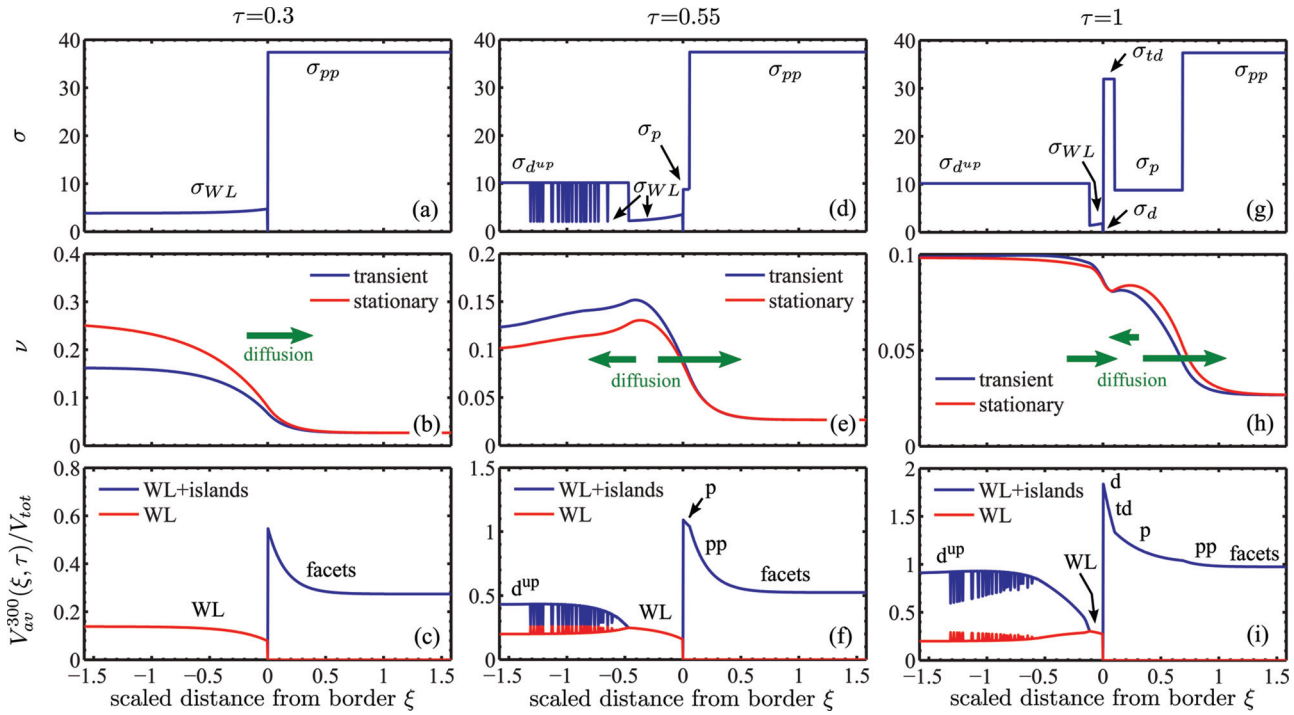

FIG. 8. (Color online) Three snapshots of the growth simulation. (a)–(c) represent the early stages of growth ($\tau = 0.3$); (d)–(f) show a later stage ($\tau = 0.55$); and (g)–(i) mark the end of the deposition ($\tau = 1$). Panels (a), (d), and (g) show the profiles of the Ge incorporation probability densities $\sigma(\xi,\tau)$; panels (b), (e), and (h) the profiles of the normalized mobile Ge surface concentration where the red curves mark the stationary solutions of the diffusion equation while the blue curves mark the transient solution at time τ. The green arrows indicate the directions of the Ge surface diffusion currents (not to scale), (c), (f), and (i) show on a linear scale the sum of the normalized Ge volumes per area incorporated into facets, islands, and WL (blue) as well as into the WL only (red). All panels are plotted versus the normalized distance from the border. The indices and labels used in all panels (pp, p, td, d, d^{up}, WL) correspond to prepyramid, pyramid, transition dome, dome on pit-patterned field, dome on unpatterned substrate region, and wetting layer, respectively. A movie with the time evolution between $\tau = 0$ and 1 is provided in the Supplemental Material (Ref. 40).

In the beginning of the Ge deposition, the Ge incorporation rate is much smaller outside the patterned field than inside [$\sigma_{WL} \ll \sigma_{pp}$, Fig. 8(a)]. As a consequence, a larger Ge surface concentration outside the patterned field than inside is established by the homogeneous Ge deposition rate. This difference in the Ge surface concentration sets up a Ge surface diffusion current into the patterned field and a corresponding Ge surface concentration gradient across the border between unpatterned and pit-patterned substrate regions as shown in Fig. 8(b) for $t = 0.3\, t_{tot}$. In Figs. 8(b), 8(e), and 8(h), the scaled transient Ge surface concentration profiles (blue lines) are shown together with the stationary ones (red lines) into which the transient profiles would evolve exponentially for the time-independent Ge incorporation probability density profiles shown in Figs. 8(a), 8(d), and 8(g). The average Ge volume V_{av}^{300} in the WL and in the islands as calculated by a time integration of the Ge incorporation current $\nu\sigma$ [Eq. (10)] is shown in Figs. 8(c), 8(f), and 8(i) for $t = 0.3$, 0.55, $1 \times t_{tot}$, respectively. In Figs. 8(c), 8(f), and 8(i), the plotted volumes were normalized to the totally deposited Ge volume $V_{tot} = n_{tot} A_u a_{Ge}^3/8$ per pattern unit cell A_u.

Due to the shape of the Ge surface concentration profile outside the patterned field (decreasing towards the border), the WL volume $V_{av,WL}^{300}$ decays towards the border [see Figs. 8(b) and 8(c)]. Thus, $V_{av,WL}^{300} + V_{av,Ge}^{300}$ reaches the threshold value for island nucleation at first at distances from the border where the Ge surface concentration gradient is vanishing. The island nucleation front propagates then towards the border. Behind the nucleation front, the surface concentration of mobile Ge is reduced due to the larger Ge incorporation probability density of the growing islands that exceeds the one of the WL. Thus, a maximum in the Ge surface concentration profile forms as shown for $\tau = 0.55$ in Fig. 8(e).

As a consequence of this maximum, $V_{av,WL}^{300} + V_{av,Ge}^{300}$ reaches the threshold value for random island nucleation earlier closer to the border, and regions without islands remain between regions where islands are already formed, resulting in an instability of the island nucleation front. In Figs. 8(d) and 8(f), this instability manifests itself by the spikes calculated in the incorporation probability density profile and the WL/island volume profiles. In Fig. 9, $V_{av,WL}^{300} + V_{av,Ge}^{300}$ normalized to the totally deposited Ge volume per pattern unit cell V_{tot} is plotted in a three-dimensional plot as a function of τ and $\xi < 0$. The ridge of the $(V_{av,WL}^{300} + V_{av,Ge}^{300})$ surface at a level of $h_{WL}^{max} = 0.4 \times V_{tot}$, shown in red, separates almost everywhere the (τ,ξ) region with growing WL (i.e., without islands) from the region where islands are already present and, thus, no further WL growth occurs. Since the Ge incorporation rate for the randomly nucleated islands is larger than that for the WL, $V_{av,WL}^{300} + V_{av,Ge}^{300}$ is decreasing with τ in this region as already discussed above. In the (τ,ξ) region with an instable nucleation front, the WL continues to grow in the stripes without islands (marked by the black lines in Fig. 9). However, in these stripes the WL growth proceeds slower than the decrease of the free Ge atoms' surface concentration. As a consequence, $V_{av,WL}^{300} + V_{av,Ge}^{300}$ is decreasing with τ also in these stripe regions without islands as shown in detail for $\xi = -1.13$ in the inset of Fig. 9. The threshold value of $V_{av,WL}^{300} + V_{av,Ge}^{300}$ for island nucleation is met not before the times lying on the $\tau(\xi)$ line connecting the blue points in Fig. 9. We conclude that an unstable nucleation front occurs in our model if the following two conditions are met: (a) increased Ge supply for WL growth in (spatial) regions of thinner WL; and (b) in time domain a fast decay of the local Ge supply that overcompensates the WL growth rate and results in a decrease of the sum $V_{av,WL}^{300} + V_{av,Ge}^{300}$ in time, thereby delaying the sum's growth up to the threshold value for island nucleation.

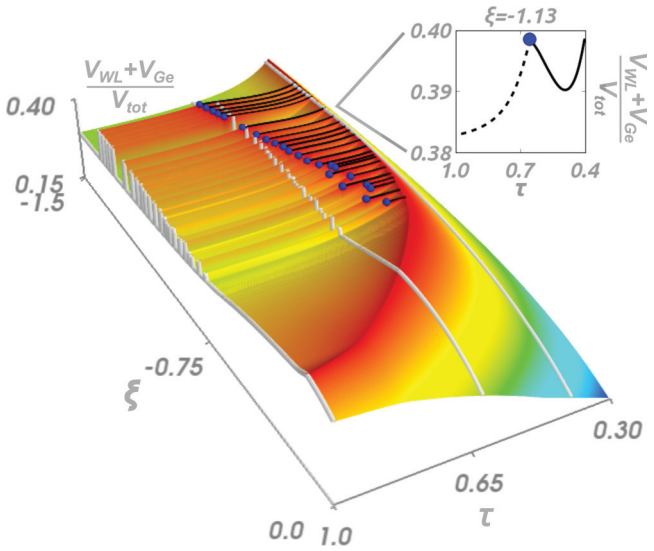

FIG. 9. (Color online) Normalized sum of the average Ge volume in the WL and in the diffusing Ge surface layer $V_{av,WL}^{300} + V_{av,Ge}^{300}$ in the unpatterned substrate part as a function of the normalized deposition time τ and normalized distance ξ from the border of the patterned field. The full line in the inset shows the τ evolution of $V_{av,WL}^{300} + V_{av,Ge}^{300}$ in a WL region at $\xi = -1.13$ without islands surrounded by regions in which random dot nucleation already occurred. The blue dot indicates the time τ, at which also in this region the threshold value of $V_{av,WL}^{300} + V_{av,Ge}^{300}$ for random island nucleation is reached. The decay shown by the broken line is due to the decay of $V_{av,Ge}^{300}$. Without insets, similar τ traces of other regions without islands are shown by the black lines superimposed on the surface plot. The white lines indicate the $V_{av,WL}^{300} + V_{av,Ge}^{300}$ profiles at $\tau = 0.4$ and 0.55.

Experimentally, the instability of the island nucleation front outside the patterned field results in only one region with significantly reduced island volume (between -20 and -15 μm, see Fig. 7), whereas the simulations predict numerous narrow regions. Considering the simplicity of our model that neglects any interactions between islands that might result in a homogenization of the island volumes, these differences in a region with unstable growth evolution are not surprising. We want to emphasize that with respect to the nucleation front instability, our model gives qualitative results only. It allows us, however, to identify the conditions formulated in the previous paragraph under which the observed instabilities can occur.

The comparison between simulation and experimental data has shown that the surface diffusion length of Ge is 4.56 $\mu m^2/s$ at $\theta_g = 650\,^{\circ}C$ and that on the patterned (unpatterned) substrate regions on average more than 11 000 (70 000) nucleation sites are visited before a Ge atom is incorporated into a growing island (see Table I). Therefore, attempts to correlate the width of the statistical island volume distribution with

that of the island-free area surrounding an island as obtained, for example, by Voronoi tesselation[49] might lead to incorrect conclusions already at moderate growth temperatures around 600 °C. In particular, the estimation of the Ge surface diffusion length by interpreting the interisland distances as a measure of the diffusion length within the deposition time of one Ge ML (Refs. 5 and 50) results in values several orders of magnitude smaller than obtained in this work[5] [taking into account the difference in growth temperatures by an exponential thermal activation of the diffusion constant with a typical activation energy of 1 eV (Refs. 51–56)], and are thus incompatible with the Ge surface transport observed in this work. For growth temperatures in the range between 400 °C and 600 °C, a poor correlation between Voronoi cell area and island volume is reported in Ref. 57 and interpreted as indication that the Ge incorporation is crucially affected by energetic factors and not univocally determined by the geometric arrangement of the nucleation sites.

Nevertheless, despite the large number of nucleation sites visited, we observe a spontaneous nucleation of secondary islands in the unstructured areas between the pits for $d_{\mathrm{pit}} \geqslant 600$ nm. In line with the assumptions of Refs. 5 and 50 used for estimating the Ge surface diffusion constant from the average distance between randomly nucleated islands, the nucleation of secondary islands on pit-patterned substrates is frequently explained in the literature by assuming a capture zone surrounding the pit, outside which the probability for a Ge atom reaching the pit is very low.[25,58,59] According to this model, secondary-island nucleation occurs, if d_{pit} becomes larger than twice the capture range. Such an interpretation is in clear contradiction to the number of nucleation sites visited by a Ge atom on the surface determined in this work. Instead, we show in the following paragraph that the secondary-island nucleation can be described quantitatively based on the diffusion model parameters determined in this work without the necessity of introducing a Ge capture zone around the nucleation sites. In our model, secondary island is the consequence of a mismatch between Ge deposition and island incorporation rates as outlined in Ref. 18. This mismatch results in the growth of a WL in the flat areas between the pits beyond the critical thickness for spontaneous island nucleation.

In our previous work,[24] it was shown that for $d_{\mathrm{pit}} \geqslant 500$ nm a clear WL signal is observed in the PL spectra measured in the centers of the patterned fields. The WL growth can be included in our model by substituting $\sigma_i + \sigma_{\mathrm{WL}}$ instead of σ_i in Eq. (9), where the values for σ_i for $d_{\mathrm{pit}} > 300$ nm can be obtained from the values listed in Table I using the scaling behavior $\sigma_i \propto 1/d_{\mathrm{pit}}^2$ obtained from Eq. (13). For σ_{WL} we use the same model and parameters as used for simulating WL growth outside the patterned field (listed in Table I). Since $\partial^2/\partial\xi^2$ vanishes several diffusion lengths L away from the border, Eq. (9) reduces to an ordinary first-order differential equation in τ that still has to be integrated numerically due to the assumed linear dependence of σ_{WL} on the WL thickness (see Sec. IV). Since σ_{WL} is to a first approximation independent of d_{pit} and $\sigma_i \propto 1/d_{\mathrm{pit}}^2$, it is immediately evident that the influence of the WL on the surface coverage ν and, thus, on the growth rates becomes more important for larger periods.

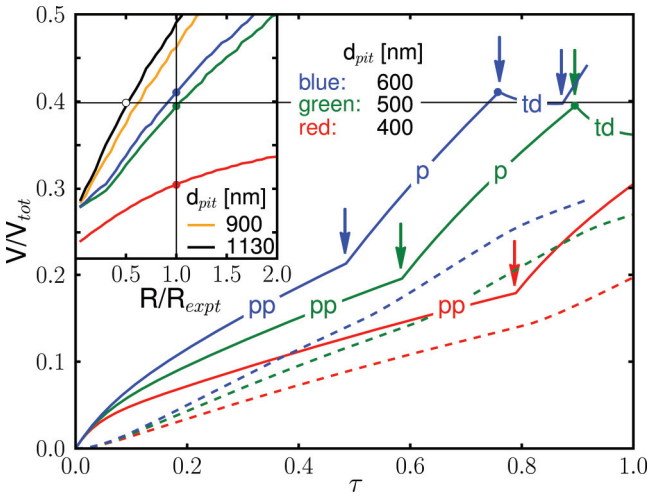

FIG. 10. (Color online) Temporal evolution of the WL thickness (broken line) and the sum of the thicknesses of WL and free Ge coverage (full lines) in flat substrate regions between the pits far away from the borders of the pit-patterned field. The color of the lines indicates the pit period d_{pit} according to the values given in the legend. The arrows show the times τ at which the shape of the islands in the pits changes from prepyramids (pp) to pyramids (p) and further to transition domes (td), and domes. The horizontal black line indicates the threshold value for random island nucleation on unpatterned substrate regions as obtained from the fit shown in Fig. 7. The full dots indicate the maximum average summed WL and free Ge coverage volume reached before dome formation. In the inset, these maximum volumes are plotted as a function of the deposition rate normalized to the one used for growing the sample with the patterned fields shown in Figs. 1 and 2 for the values of d_{pit} indicated in the plot.

In Fig. 10, the time dependence of the WL thickness (broken lines) and the sum of WL thickness and free Ge coverage (full lines) calculated for the center of the patterned fields are shown in relative units (as V/V_{tot}, where V stands for $V_{\mathrm{av,WL}}^{300}$ and $V_{\mathrm{av,WL}}^{300} + V_{\mathrm{av,Ge}}^{300}$) for the three pattern periods indicated in the plot. In the traces for the summed thicknesses of WL and free Ge coverage, clear kinks appear (marked by arrows) whenever the island type at the pit positions, and, thus, the average Ge incorporation probability density instantaneously change. The various island types growing in the pits are indicated (pp, p, td) in the sections between the arrows.

Figure 10 shows that for $d_{\mathrm{pit}} = 600$ nm the critical thickness for spontaneous island nucleation as obtained from the fitting described in Sec. IV and indicated by the horizontal black line in Fig. 10 is clearly exceeded by the summed WL and the free surface Ge coverage at the end of the pyramid growth phase, whereas for $d_{\mathrm{pit}} = 500$ and 400 nm this threshold is not crossed during ordered island growth. These results are in excellent agreement with the AFM images shown in Fig. 1, where no secondary islands are observed for $d_{\mathrm{pit}} \leqslant 500$ nm and a large number for $d_{\mathrm{pit}} \geqslant 600$ nm. Thus, we conclude that, in complete analogy to the unpatterned substrate areas, also in the flat substrate regions between the pits an overcritically thick, two-dimensional Ge layer is responsible for secondary-island nucleation.

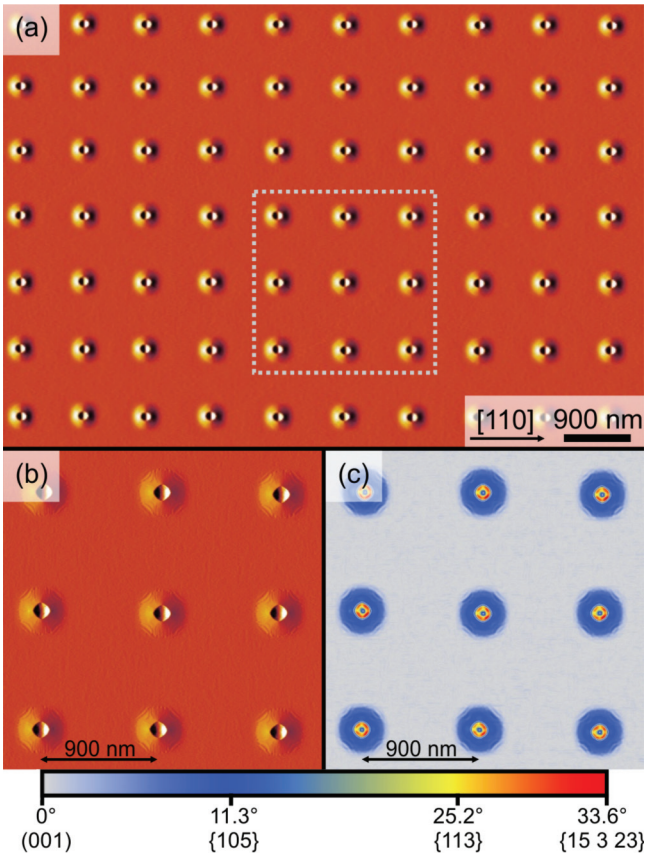

FIG. 11. (Color online) AFM micrographs of a pit-patterned sample after deposition of 45 nm of Si at 450 °C–550 °C and deposition of 5.2 Å of Ge at 650 °C at a growth rate of 0.015 Å/s, taken at a pit-patterned field with period $d_{pit} = 900$ nm. (b) and (c) show the region marked by a broken line in (a) at larger magnification. In (c), a surface-angle image mode was used, where the color coding represents the local surface slope with respect to the (001) surface. The color bar is chosen in a way that the {105}, {113}, {15 3 23} dome facets appear as blue, yellow, and red, respectively. Evidently, all islands are domes.

It is important to stress that the appearance of secondary islands between the pits can be avoided also for fields with large d_{pit} by reducing the Ge deposition rate. In the inset of Fig. 10, the maxima of the simulated summed WL thicknesses and free Ge surface coverages are plotted as a function of the growth rate normalized to the rate R_{expt} used for growing the samples shown in Figs. 1 and 2. Reducing the rate only by a factor of 2 shifts the maximum of the summed WL thickness and Ge surface coverage far below the threshold value for spontaneous island nucleation also for a pit period of $d_{pit} = 600$ m. For such a small deposition rate, our simulations predict for pattern periods up to $d_{pit} = 1130$ nm no secondary-island nucleation as indicated by the black trace in the inset of Fig. 10, which at $R/R_{expt} = 0.5$ is equal to the threshold value (marked with a circle).

For an experimental verification of these predictions, ordered islands were grown on a substrate with a pit period of 900 nm reducing the Ge deposition rate to 0.015 Å/s (i.e., to $0.6R_{expt}$) and the totally deposited Ge coverage to 3.86 ML in order to avoid superdome formation. All other growth parameters were set to the same values as used for growing the islands shown in Figs. 1 and 2. In Fig. 11, it is shown that for this growth rate perfectly ordered dome islands with $d_{pit} = 900$ nm are obtained without secondary islands, in agreement with the results of our simulations shown in the inset of Fig. 10 by the orange line, which stays just below the threshold value for spontaneous island nucleation (indicated by the black horizontal line) at $R/R_{expt} = 0.6$.

VI. SUMMARY

The shapes and volumes of SiGe islands show a pronounced dependence on the islands' distance from the border between unpatterned and pit-patterned Si(001) substrate areas used for establishing ordered epitaxial island growth. A surface diffusion model was set up to describe the transport of Ge adatoms deposited during MBE growth from outside into the patterned substrate regions. The different types of growing Ge islands and the WL are included as Ge sinks with different Ge incorporation probability. By fitting the simulated volume versus distance dependence to the observed one, the Ge incorporation probability densities for the various island types inside and outside the patterned field, that of the WL, as well as the Ge surface diffusion coefficient, were quantitatively determined for a growth temperature of 650 °C. Based on these values, it was shown that a Ge adatom on average visits more that 10 000 pits before it is incorporated into an island evolving in a pit. These findings clearly rule out a diffusion range smaller than the pit-pattern unit cell area as the reason for secondary-island nucleation between pits, which is frequently observed at this growth temperature. Instead, the Ge deposition rate was identified in theory and experiment as the most crucial parameter by which secondary-island nucleation in substrate regions between pits can be controlled.

ACKNOWLEDGMENTS

The work was supported by the Austrian Science Fund FWF (Contracts No. SFB02502 and No. SFB02512), by GMe, Austria, and by the Austrian Nanoinitiative (Projects No. 815802 and No. 815803). In addition, M. Brehm acknowledges support from the FWF under Project No. J3328-N19.

APPENDIX: NUMERICAL METHODS

In Eq. (9), the incorporation term σ depends on τ and ξ via the island volumes V_{av} calculated according to Eq. (10) as discussed in detail in Sec. V. For a numerical solution of Eq. (9), we discretize the time to obtain

$$\nu(\xi,\tau_{j+1}) = \Delta\tau + \left\{1 + \Delta\tau\left[\frac{\partial^2}{\partial\xi^2} - \sigma[V_{av}(\xi,\tau_j)]\right]\right\}\nu(\xi,\tau_j), \tag{A1}$$

where $\Delta\tau = \tau_{j+1} - \tau_j$ denotes the time step. For a known initial condition $\nu(\xi,\tau_j)$ and a given scaled incorporation probability density profile $\sigma[V_{av}(\xi,\tau_j)]$, Eq. (A1) is used to calculate $\nu(\xi,\tau_{j+1})$.

The first term on the right-hand side ($\Delta\tau$), which accounts for the spatially constant deposition rate, makes Eq. (A1) an inhomogeneous difference equation. To solve Eq. (A1), we take advantage of its linearity in ν and split up the general solution $\nu(\xi,\tau_j) = \nu_{ih}(\xi,\tau_j) + \nu_h(\xi,\tau_j)$ into a particular

solution $\nu_{ih}(\xi,\tau_j)$ of Eq. (A1) and the solution $\nu_h(\xi,\tau_j)$ of Equation's (A1) homogeneous counterpart

$$\nu_h(\xi,\tau_{j+1}) = \left\{1 + \Delta\tau\left[\frac{\partial^2}{\partial\xi^2} - \sigma[V_{\mathrm{av}}(\xi,\tau_j)]\right]\right\}\nu_h(\xi,\tau_j), \tag{A2}$$

where $\nu_h(\xi,\tau_j)$ has to be chosen so that given boundary conditions $\nu^j(\xi) = \nu_{ih}(\xi,\tau_j) + \nu_h(\xi,\tau_j)$ are fulfilled.

As particular inhomogeneous solution we take the stationary one defined by $\nu_{ih,s}(\xi,\tau_{j+1}) = \nu_{ih,s}(\xi,\tau_j)$, for which Eq. (A1) simplifies to

$$\mathcal{O}^j\nu^j_{ih,s}(\xi) = -1, \quad \text{where} \quad \mathcal{O}^j \equiv \left[\frac{\partial^2}{\partial\xi^2} - \sigma[V_{\mathrm{av}}(\xi,\tau_j)]\right]. \tag{A3}$$

Since the stationary, inhomogeneous solution $\nu^j_{ih,s}(\xi)$ depends on the time only via $\sigma(V_{\mathrm{av}})$'s time dependence, we have used the superscript j in Eq. (A3) to indicate this parametric time dependence of $\nu^j_{ih,s}(\xi)$ and make a distinction from the intrinsic (diffusive) time dependence of $\nu_h(\xi,\tau_j)$, which varies with time also for time independent $\sigma(V_{\mathrm{av}})$ according to Eq. (A2). In Figs. 8(b), 8(e), and 8(h), $\nu^j_{ih,s}$ is shown by the red lines.

According to our choice of $\nu^j_{ih,s}(\xi)$ as particular inhomogeneous solution, the diffusive time dependence is completely contained in $\nu_h(\xi,\tau_j)$ as described by Eq. (A2). This time dependence is governed by the operator $\mathcal{O}^j$ defined in Eq. (A3), which is formally equivalent to the *negative* of the Hamilton operator of a single particle in a one-dimensional, non-negative scalar potential σ. We exploit this analogy and expand the initial condition $\nu^j(\xi) - \nu^j_{ih,s}(\xi) = \sum_n c^j_n\nu^j_n(\xi)$ into a complete set of eigenfunctions $\nu^j_n(\xi)$ of the operator $\mathcal{O}^j$ defined by

$$\mathcal{O}^j\nu^j_n(\xi) = \lambda^j_n\nu^j_n(\xi) \tag{A4}$$

with only *negative* eigenvalues λ^j_n. It is evident then from Eq. (A2) that the expansion coefficients c^j_n for $\nu_h(\xi,\tau_j)$ decay during $\Delta\tau$ according to

$$c^{j+1}_n = \left(1 - \Delta\tau\left|\lambda^j_n\right|\right)c^j_n, \tag{A5}$$

allowing a straightforward calculation of the total scaled Ge concentration profile at time step τ_{j+1}:

$$\nu(\xi,\tau_{j+1}) = \nu^j_{ih,s}(\xi) + \sum_n c^{j+1}_n\nu^j_n(\xi). \tag{A6}$$

For solving Eqs. (A3) and (A4), spatially periodic boundary conditions were assumed with a period much larger than all scaled decay lengths observed in the experiments as verified *a posteriori*. Next, Eqs. (A3) and (A4) were transformed into Fourier space and solved after proper truncation of $\mathcal{O}^j$ into a finite matrix by matrix inversion and diagonalization, respectively. The maximum scaled wave-vector magnitude $|\kappa_m|$ included in the Fourier transformation and, thus, in the matrix equations depends on the spatial resolution $\Delta\xi$ aimed at in the numerical calculation of $\nu(\xi,\tau)$ via the Nyquist Theorem ($|\kappa_m| = \pi/\Delta\xi$).

Finally, also the scaled time resolution of the simulation $\Delta\tau$ is tied to $|\kappa_m|$ since the Fourier components of $\nu(\xi,\tau)$ with wave vector $|\kappa| \gg \sqrt{\sigma_m}$ decay with eigenvalues $\lambda \approx -\kappa^2$ according to Eqs. (A4) and (A5). Here, σ_m denotes the maximum of the Ge capture probability density $\sigma[V_{\mathrm{av}}(\xi,\tau_j)]$. However, the time discretization used to derive Eq. (A1) is only a good approximation if $\Delta\tau$ is small compared to the time scale of changes in $\nu(\xi,\tau)$. Using Eq. (A5), this requirement can be quantified as $\Delta\tau \ll 1/|\lambda_m| \approx 1/\kappa^2_m$. Thus, for required temporal and spatial resolutions $\Delta\tau$ and $\Delta\xi$, Fourier components up to $|\kappa_m| \gg \max(1/\sqrt{\Delta\tau},\pi/\Delta\xi)$ have to be included in the simulation of $\nu(\xi,\tau)$.

As further illustration of the numerical methods used for solving Eq. (9), a flowchart is provided in the Supplemental Material.[40]

*Present address: Institute for Integrative Nanosciences, Leibniz Institute for Solid State and Materials Research, D-01171 Dresden, Germany.

†thomas.fromherz@jku.at

[1] L. Goldstein, F. Glas, J. Y. Marzin, M. N. Charasse, and G. L. Roux, Appl. Phys. Lett. **47**, 1099 (1985).

[2] S. Guha, A. Madhukar, and K. C. Rajkumar, Appl. Phys. Lett. **57**, 2110 (1990).

[3] Y. W. Mo, D. E. Savage, B. S. Swartzentruber, and M. G. Lagally, Phys. Rev. Lett. **65**, 1020 (1990).

[4] D. J. Eaglesham and M. Cerullo, Phys. Rev. Lett. **64**, 1943 (1990).

[5] T. I. Kamins, E. C. Carr, R. S. Williams, and S. J. Rosner, J. Appl. Phys. **81**, 211 (1997).

[6] G. Jin, J. L. Liu, and K. L. Wang, Appl. Phys. Lett. **76**, 3591 (2000).

[7] T. I. Kamins and R. S. Williams, Appl. Phys. Lett. **71**, 1201 (1997).

[8] O. G. Schmidt, N. Y. Jin-Phillipp, C. Lange, U. Denker, K. Eberl, R. Schreiner, H. Gräbeldinger, and H. Schweizer, Appl. Phys. Lett. **77**, 4139 (2000).

[9] G. Biasiol, A. Gustafsson, K. Leifer, and E. Kapon, Phys. Rev. B **65**, 205306 (2002).

[10] E. Pelucchi, V. Dimastrodonato, A. Rudra, K. Leifer, E. Kapon, L. Bethke, P. A. Zestanakis, and D. D. Vvedensky, Phys. Rev. B **83**, 205409 (2011).

[11] Z. Zhong, A. Halilovic, T. Fromherz, F. Schäffler, and G. Bauer, Appl. Phys. Lett. **82**, 4779 (2003).

[12] B. Yang, F. Liu, and M. G. Lagally, Phys. Rev. Lett. **92**, 025502 (2004).

[13] Z. Zhong, W. Schwinger, F. Schäffler, G. Bauer, G. Vastola, F. Montalenti, and L. Miglio, Phys. Rev. Lett. **98**, 176102 (2007).

[14] C. Dais, H. H. Solak, E. Müller, and D. Grützmacher, Appl. Phys. Lett. **92**, 143102 (2008).

[15] M. Grydlik, M. Brehm, F. Hackl, H. Groiss, T. Fromherz, F. Schäffler, and G. Bauer, New J. Phys. **12**, 063002 (2010).

[16] G. Vastola, M. Grydlik, M. Brehm, T. Fromherz, G. Bauer, F. Boioli, L. Miglio, and F. Montalenti, Phys. Rev. B **84**, 155415 (2011).

[17] R. Bergamaschini, J. Tersoff, Y. Tu, J. J. Zhang, G. Bauer, and F. Montalenti, Phys. Rev. Lett. **109**, 156101 (2012).

[18]M. Grydlik, G. Langer, T. Fromherz, F. Schäffler, and M. Brehm, Nanotechnology **24**, 105601 (2013).
[19]J.-N. Aqua, I. Berbezier, L. Favre, T. Frisch, and A. Ronda, Phys. Rep. **522**, 59 (2013).
[20]V. Jovanović, C. Biasotto, L. Nanver, J. Moers, D. Grützmacher, J. Gerharz, G. Mussler, J. van der Cingel, J. Zhang, G. Bauer, O. Schmidt, and L. Miglio, IEEE Electron Device Lett. **31**, 1083 (2010).
[21]M. Brehm, M. Grydlik, F. Hackl, E. Lausecker, T. Fromherz, and G. Bauer, Nano. Res. Lett. **5**, 1868 (2010).
[22]E. Lausecker, M. Brehm, M. Grydlik, F. Hackl, I. Bergmair, M. Mühlberger, T. Fromherz, F. Schäffler, and G. Bauer, Appl. Phys. Lett. **98**, 143101 (2011).
[23]L. Miglio and F. Montalenti, in *Silicon-germanium (SiGe) Nanostructures*, edited by Y. Shiraki and N. Usami (Woodhead, Cambridge, 2011), p. 211.
[24]F. Hackl, M. Grydlik, M. Brehm, H. Groiss, F. Schäffler, T. Fromherz, and G. Bauer, Nanotechnology **22**, 165302 (2011).
[25]Z. Zhong, P. Chen, Z. Jiang, and G. Bauer, Appl. Phys. Lett. **93**, 043106 (2008).
[26]G. S. Kar, S. Kiravittaya, M. Stoffel, and O. G. Schmidt, Phys. Rev. Lett. **93**, 246103 (2004).
[27]S. Kiravittaya, A. Rastelli, and O. G. Schmidt, Appl. Phys. Lett. **87**, 243112 (2005).
[28]J. Stangl, A. Hesse, V. Holý, Z. Zhong, G. Bauer, U. Denker, and O. G. Schmidt, Appl. Phys. Lett. **82**, 2251 (2003).
[29]M. Stoffel, G. S. Kar, U. Denker, A. Rastelli, H. Sigg, and O. G. Schmidt, Phys. E (Amsterdam) **23**, 421 (2004).
[30]M. Brehm, M. Grydlik, H. Lichtenberger, T. Fromherz, N. Hrauda, W. Jantsch, F. Schäffler, and G. Bauer, Appl. Phys. Lett. **93**, 121901 (2008).
[31]M. Brehm, M. Grydlik, H. Groiss, F. Schäffler, T. Fromherz, and G. Bauer, J. Appl. Phys, **109**, 123505 (2011).
[32]T. I. Kamins, G. Medeiros-Ribeiro, D. A. A. Ohlberg, and R. S. Williams, J. Appl. Phys. **85**, 1159 (1999).
[33]Z. Zhong, O. G. Schmidt, and G. Bauer, Appl. Phys. Lett. **87**, 133111 (2005).
[34]M. A. Lutz, R. M. Feenstra, P. M. Mooney, J. Tersoff, and J. O. Chu, Surf. Sci. **316**, L1075 (1994).
[35]A. Rastelli and H. von Känel, Surf. Sci. **515**, L493 (2002).
[36]A. Vailionis, B. Cho, G. Glass, P. Desjardins, D. G. Cahill, and J. E. Greene, Phys. Rev. Lett. **85**, 3672 (2000).
[37]F. M. Ross, R. M. Tromp, and M. C. Reuter, Science **286**, 1931 (1999).
[38]F. Montalenti, P. Raiteri, D. B. Migas, H. von Känel, A. Rastelli, C. Manzano, G. Costantini, U. Denker, O. G. Schmidt, K. Kern, and L. Miglio, Phys. Rev. Lett. **93**, 216102 (2004).
[39]G. Medeiros-Ribeiro, A. M. Bratkovski, T. I. Kamins, D. A. A. Ohlberg, and R. S. Williams, Science **279**, 353 (1998).
[40]See Supplemental Material at http://link.aps.org/supplemental/10.1103/PhysRevB.88.115311 for overlapping AFM micrographs, for a movie, and for a flowchart illustrating the numerical methods.
[41]The existence of stable dome sizes might depend on the size and the form of the pits etched into the substrates, as it is clearly and reproducibly observed in this work, but not, for example, in Ref. 60.
[42]L. Tsybeskov and D. Lockwood, Proc. IEEE **97**, 1284 (2009).
[43]P. J. Dean, J. R. Haynes, and W. F. Flood, Phys. Rev. **161**, 711 (1967).
[44]M. Brehm, F. Montalenti, M. Grydlik, G. Vastola, H. Lichtenberger, N. Hrauda, M. J. Beck, T. Fromherz, F. Schäffler, L. Miglio, and G. Bauer, Phys. Rev. B **80**, 205321 (2009).
[45]F. Boioli, R. Gatti, M. Grydlik, M. Brehm, F. Montalenti, and L. Miglio, Appl. Phys. Lett. **99**, 033106 (2011).
[46]F. M. Ross, J. Tersoff, and R. M. Tromp, Phys. Rev. Lett. **80**, 984 (1998).
[47]M. J. Beck, A. van de Walle, and M. Asta, Phys. Rev. B **70**, 205337 (2004).
[48]J. J. Moré, in *Numerical Analysis*, edited by G. Watson, Lecture Notes in Mathematics Vol. 630 (Springer, Berlin, 1978), pp. 105–116.
[49]The surface is divided into sectors that are associated with each island and are defined as the set of points that are closer to a given island rather than to any other.
[50]S. Miyamoto, O. Moutanabbir, E. E. Haller, and K. M. Itoh, Phys. Rev. B **79**, 165415 (2009).
[51]X. R. Qin, B. S. Swartzentruber, and M. G. Lagally, Phys. Rev. Lett. **85**, 3660 (2000).
[52]Z.-Y. Lu, C.-Z. Wang, and K.-M. Ho, Phys. Rev. B **62**, 8104 (2000).
[53]Z.-Y. Lu, C. Wang, and K. Ho, Surf. Sci. **506**, L282 (2002).
[54]L. M. Sanders, R. Stumpf, T. R. Mattsson, and B. S. Swartzentruber, Phys. Rev. Lett. **91**, 206104 (2003).
[55]L. Huang, F. Liu, and X. G. Gong, Phys. Rev. B **70**, 155320 (2004).
[56]E. Bussmann and B. S. Swartzentruber, Phys. Rev. Lett. **104**, 126101 (2010).
[57]F. Ratto, A. Locatelli, S. Fontana, S. Kharrazi, S. Ashtaputre, S. K. Kulkarni, S. Heun, and F. Rosei, Phys. Rev. Lett. **96**, 096103 (2006).
[58]P. A. Mulheran and J. A. Blackman, Phys. Rev. B **53**, 10261 (1996).
[59]R. Bergamaschini, F. Montalenti, and L. Miglio, Nano. Res. Lett. **5**, 1873 (2010).
[60]J. J. Zhang, F. Montalenti, A. Rastelli, N. Hrauda, D. Scopece, H. Groiss, J. Stangl, F. Pezzoli, F. Schäffler, O. G. Schmidt, L. Miglio, and G. Bauer, Phys. Rev. Lett. **105**, 166102 (2010).